Preprint Cambridge Centre for Computational Chemical Engineering ISSN 1473 – 4273

A coupled CFD-population balance approach for nanoparticle synthesis in turbulent reacting flows

Jethro Akroyd [1], Alastair J. Smith [1], Raphael Shirley [1],
Laurence R. McGlashan [1], Markus Kraft [1]

released: 15 April 2011

[1] Department of Chemical Engineering
and Biotechnology
University of Cambridge
New Museums Site
Pembroke Street
Cambridge, CB2 3RA
UK
E-mail: mk306@cam.ac.uk

Preprint No. 99

Keywords: Mathematical modelling, Simulation, Turbulence, Chemical reactors, Population balance, CFD

Edited by
Computational Modelling Group
Department of Chemical Engineering and Biotechnology
University of Cambridge
New Museums Site
Pembroke Street
Cambridge CB2 3RA
United Kingdom

Fax: + 44 (0)1223 334796
E-Mail: c4e@cam.ac.uk
World Wide Web: http://como.cheng.cam.ac.uk/

Abstract

This paper investigates the first part of a two-stage methodology for the detailed fully coupled modelling of nanoparticle formation in turbulent reacting flows. We use a projected fields (PF) method to approximate the joint composition probability density function (PDF) transport equation that describes the evolution of the nanoparticles. The method combines detailed chemistry and the method of moments with interpolative closure (MoMIC) population balance model in a commercial computational fluid dynamics (CFD) code. We show details of the implementation and present an extensive set of numerical experiments and validation. We consider the example of the chloride process for the industrial synthesis of titania. We show good agreement with experimental data and present fully coupled detailed chemistry CFD simulations of nanoparticle formation in a representative 'slot' reactor geometry. The simulations show that inception occurs in a mixing zone near the reactor inlets. Most of the nanoparticle mass is due to surface growth downstream of the mixing zone with a narrower size distribution occurring in the regions of higher surface growth. The predicted temperature and particle properties are compared to a perfect mixing case. The implications for the second part of the methodology, where it is proposed to post process the data using a more detailed particle model, are discussed critically.

Contents

1 Introduction

Nanoparticle synthesis in turbulent reacting flows is a key field of engineering research [48, 56, 57]. This paper considers the example of titania nanoparticles. Titania (TiO_2) represents a three-quarters share of the global white pigment market (1996) [25] and equates to annual sales of £7 billion (5 million tonnes) in over 170 countries (2009) [30]. The industrial production of titania usually occurs via the *chloride process* in which titanium tetrachloride $TiCl_4$ is oxidised in either a flame [51] or by stage-wise addition to an oxygen plasma [13, 41] to produce TiO_2 particles. The pigmentary properties of the product require tight control of the particle size, shape and crystal phase. Although widely used, the chloride process is not well understood and process optimisation is often empirical.

The chloride process is exothermic and exhibits strong coupling between the chemistry, the temperature and the flow in the reactor. Detailed insight requires an understanding of the evolution of the product within the reactor. Any detailed process model must consider the design of the reactor and account for the effect of turbulence on the rates of mixing and reaction. It must contain a sufficient description of the gas and solid-phase chemistry. It must include a population balance to describe the evolution of the product and must resolve the coupling between all these processes.

Turbulent flow methods typically separate the velocity and scalar quantities (such as species concentration) into resolved and unresolved components. For example, Favre-averaged Navier-Stokes methods solve transport equations for density-averaged components, but need to close terms arising from unresolved fluctuating components. In reacting cases, the source terms in the material and energy balance equations are left unclosed and must be modelled. Many turbulent reaction models have been studied [18, 34, 45]. Transported probability density function (PDF) methods [28] are applicable to all flows and offer the key advantage that the chemical source term does not need to be closed. However, Monte Carlo solution techniques are typically required [46]. These may be computationally expensive and not necessarily suited to the computational fluid dynamics (CFD) software that would often be the method of choice for turbulent flow simulations.

A recent turbulent reaction method amenable to existing CFD codes is the Direct Quadrature Method of Moments using the Interaction by Exchange with the Mean micromixing model (DQMoM-IEM). The method was first suggested by Fox [18]. A joint composition PDF transport equation is approximated using a weighted discretisation in composition space and the IEM micromixing model [70]. An arbitrary moment set is used to derive transport equations for the approximated PDF that guarantee to reproduce consistent transport of the moments within this set. The method has been applied to precipitation reactions [22, 71], stabilised turbulent methane-hydrogen flames [67] and turbulent combustion in industrial furnaces and gasifiers [14]. Recent studies have considered the numerical implementation [1] and efficiency [2] of the method in detail for a prescribed moment set. In the context of turbulent reacting flows, DQMoM-IEM is a projected fields (PF) method and this is the terminology we adopt in this paper.

The **purpose of this paper** is to investigate the first part of a two-stage methodology for the detailed modelling of nanoparticle formation in turbulent reacting flows:

- The first-stage extends the PF method to combine detailed gas-phase chemistry and a population balance for CFD simulations involving *full coupling* between the flow, chemistry and particles undergoing simultaneous inception, coagulation and surface growth. The objective is to achieve a reasonable description of the velocity field and gas-phase composition PDF for minimum computational effort.
- The second-stage models the evolution of the nanoparticles using a *detailed* population balance model to post processes the gas-phase composition data. There is free choice of the population balance model because the gas-phase data already include the coupling to the population, negating the need to re-solve the chemistry or flow.

This approach is well established for soot simulations in 1D laminar flames [40, 64, 79] and has been applied to titania formation in turbulent diffusion flames [31] (where the coupling is ignored). We follow the approach for soot and use the method of moments with interpolative closure (MoMIC) [20] to describe the population balance.

The paper is organised as follows. Section 2 introduces the key aspects of the kinetic model of the gas and solid-phase chemistry, the choice of population balance model and the PF method. Section 3 summarises the numerical implementation of the method and the coupling to the CFD code. Section 4 investigates the performance of the model against test case and experimental data, and demonstrates the application of the method to the full reacting case for a representative industrial titania reactor.

2 Theoretical background

This section introduces key aspects of the kinetic model for the formation of titania, the choice of population balance model and the PF method.

2.1 Kinetic models for titania formation

Typical industrial conditions for the production of titania via the chloride process are a stoichiometric binary mixture of $TiCl_4$ and O_2 plus additives reacting at 1500–2000 K. The process is difficult to investigate experimentally under these conditions. It has been widely studied at milder conditions, but understanding remains incomplete.

Ghoshtagore [23] investigated the addition of $TiCl_4$ to a TiO_2 film. The surface reaction was suggested to display an Eley-Rideal dependence on $TiCl_4$ and O_2 at 673–1120 K. Pratsinis et al. [50] studied the oxidation of $TiCl_4$ vapour at 973–1273 K. The reaction was first-order in $TiCl_4$ and approximately zero-order in O_2 up to ten-fold excess O_2. The kinetics are reported in terms of a global reaction. Pratsinis and Spicer [49] compare the overall kinetics with a gas-phase oxidation rate inferred from the difference between the overall rate [50] and a surface growth rate [23] assuming a monodisperse population of spherical particles. The study shows that surface reaction has a significant effect on the particle diameter. Later studies using more detailed population balance models draw similar conclusions [29, 38, 39, 68].

West et al. [75, 76] argue that more detailed understanding of the chemical mechanism may yield deeper insight. They present the first thermodynamically consistent mechanism for the high temperature oxidation of $TiCl_4$. The reaction is suggested to proceed via titanium oxychloride species. Unknown thermochemical data are estimated by density functional theory based quantum calculations. Subsequent investigations present an updated mechanism [77] and consider the role of aluminium (used as an additive) [62].

Mehta et al. [37] compare the inception behaviour of the mechanisms from Pratsinis and Spicer [49] and West et al. [77]. They show that the choice of mechanism causes inception to occur at different spatial locations in simulations of a turbulent flame and would be expected to significantly influence the sintering behaviour predicted by each simulation. This is consistent with recent observations [63] where the choice of inception mechanism is noted to strongly affect simulations of Pratsinis' original experiment [50].

2.1.1 Model equations

The investigation in this paper uses the gas-phase chemistry of West et al. [77, note that West et al. supply the mechanism as supplementary material]. The mechanism includes 28 gas-phase plus 1 solid-phase species and 66 reactions.

Inception and surface reaction are treated slightly differently from West et al. [77]. This choice is based on theoretical investigations of TiO_2 growth and fits to experimental data discussed in a paper to follow [63]. All bimolecular collisions between titanium oxychloride species are treated as inception steps

$$\begin{aligned} \mathrm{Ti}_{x_\alpha}\mathrm{O}_{y_\alpha}\mathrm{Cl}_{z_\alpha} + \mathrm{Ti}_{x_\beta}\mathrm{O}_{y_\beta}\mathrm{Cl}_{z_\beta} \longrightarrow{}& \left(x_\alpha + x_\beta\right)\mathrm{TiO}_{2\,(\mathrm{s})} \\ &+ \left(\frac{y_\alpha + y_\beta}{2} - x_\alpha - x_\beta\right)\mathrm{O}_2 + \left(\frac{z_\alpha + z_\beta}{2}\right)\mathrm{Cl}_2\,, \qquad x, y, z \geq 1\,, \end{aligned} \tag{1}$$

with the molecular collision diameter is taken as 0.65 nm [77]. Surface growth is treated as a second-order reaction

$$\mathrm{TiCl}_4 + \mathrm{O}_2 \longrightarrow \mathrm{TiO}_2 + 2\,\mathrm{Cl}_2\,, \tag{2}$$

subject to the rate expression

$$\begin{aligned} \frac{\mathrm{d}\left[\mathrm{TiO}_2\right]}{\mathrm{d}t} &= k_\mathrm{s}\, A \left[\mathrm{TiCl}_4\right]\left[\mathrm{O}_2\right], \\ k_\mathrm{s} &= 200\ \exp\!\left(\frac{-50\,\mathrm{kJ/mol}}{RT}\right)\frac{\mathrm{m}}{\mathrm{s}}\cdot\frac{\mathrm{m}^3}{\mathrm{mol}}\,, \end{aligned} \tag{3}$$

where A is the surface area per unit volume of the TiO_2 population. Equation (3) assumes fixed reaction orders with respect to $TiCl_4$ and O_2, but is sufficient for the purpose of this study. Alternatives to this assumption are discussed in detail by Shirley et al. [63]. The full model has 29 species and 172 (66 gas-phase, 105 inception, 1 surface) reactions.

2.2 Population balance models

The basic population balance equation describing the evolution of a particle distribution is the Smoluchowski coagulation equation. Population balances are discussed in detail by Ramkrishna [52] and their modelling within reacting flows is reviewed by Rigopoulos [55]. The relative advantages of the main approaches that have been applied to models of nanoparticle formation are discussed below.

The method of moments (MoM) solves for low-order moments of the distribution. The actual distribution remains unknown and the moment equations are typically unclosed. One approach is to assume the form of the distribution [47]. This has been applied to CFD simulations of aerosols [21]. The two main closures applied to nanoparticles are the method of moments with interpolative closure (MoMIC) [19, 20] and the quadrature method of moments (QMoM) [36].

MoMIC closes fractional-order moments that arise due to coagulation and surface growth processes by interpolation among known whole-order moments. It is efficient and widely favoured for problems involving populations and flow. For example, a modified version [53] of PREMIX [32] has been used for a number of fully coupled 1D laminar flame simulations [3, 64, 79]. Good accuracy in the first moment is reported for organic [6] and inorganic [26] systems. Most implementations are univariate and assume spherical particles, but MoMIC has also been extended to study aggregate particle growth [5, 42].

QMoM uses a quadrature method to approximate the distribution as a set of weighted particles. The method was developed for univariate distributions, but has been extended to bivariate cases [78]. A later approach was to transport the parameters of the weighted particle approximation in the direct quadrature method of moments (DQMoM) [35]. DQMoM is easily extended to multi-variate cases, but can be numerically challenging [80].

Sectional methods approximate the distribution by discretising the particle state space. Moving sectional methods were introduced to control numerical diffusion and have been been applied to several titania studies [65, 68]. Bivariate formulations are possible and have been used to investigate the sintering of silica and titania [29, 61]. A technique to couple CFD simulations to a Lagrangian joint composition discretised population balance PDF method has been proposed [54, 69]. Sectional methods resolve the full distribution, but are more expensive than moment methods.

Monte Carlo methods simulate the evolution of the particle distribution as a series of discrete events acting on an ensemble of stochastic particles. They efficiently extend to multi-variate cases and have been proved to converge to the solution of the governing population balance [17, 72]. A number of stochastic algorithms have been developed [15, 16] and refined [24, 43, 44, 73, 74] for nanoparticle applications. They may be used to post process existing data [40, 64, 79] or coupled directly to chemistry models [9, 11]. Multi-variate implementations have introduced active site models where particle growth is a function of aggregate composition [10, 12], or the sintering of individual particles is calculated using the connectivity within each aggregate [59, 60]. Recent applications include simulation of the aggregate behaviour of soot on Titan [33]. Stochastic methods allow detailed models and are an attractive option for post processing existing data, but are often expensive and not easily coupled to CFD.

2.2.1 Model equations

MoMIC is used to describe the evolution of a truncated set of whole-order moments of a distribution of spherical particles undergoing inception, coagulation and surface growth in a fully coupled turbulent reacting flow simulation. The coupling primarily depends on the mass of the population (proportional to the first moment). MoMIC is reasonably accurate for the first moment [6, 26] and is a judicious compromise between speed and accuracy.

Balthasar et al. [7] show that the turbulent enhancement of the collision frequency [58] is small compared to Brownian coagulation under a wide range of conditions. They neglect the turbulent enhancement and we invoke the same approximation here. They show that the moments of a particle distribution may be included in a consistent PDF formulation. In conjunction with the numerical treatment described in section 3, MoMIC can be implemented directly within the PF method without further changes.

MoMIC is described in detail by Frenklach [19] and is summarised below. The particle population is described by the number density moments of the size distribution

$$M_r = \sum_{i=1}^{\infty} i^r n_i \,, \quad r = 0, \ldots, U-1 \,, \tag{4}$$

where n_i is the number density of particles of size i and mass $m_i = i \cdot m_1$, m_1 is the mass of the smallest unit occurring in the population and U is the number of moments in the truncated set. The low-order moments have simple physical interpretations

$$M_0 = \sum_{i=1}^{\infty} n_i = n \,, \tag{5}$$

$$M_1 = \sum_{i=1}^{\infty} i \cdot n_i = f_\mathrm{v} \frac{\rho_\mathrm{s}}{m_1} \,, \tag{6}$$

where n is the total number density, f_v is the volume fraction occupied by the population and ρ_s is the particle density.

The population dynamics are governed by a population balance equation describing the effect of collisions between particles of the same type

$$\frac{\mathrm{d}n_i}{\mathrm{d}t} = \frac{1}{2} \sum_{j=1}^{i-1} \beta_{j,i-j} n_j n_{i-j} - \sum_{j=1}^{\infty} \beta_{i,j} n_i n_j \,, \tag{7}$$

where $\beta_{i,j}$ is a frequency factor describing the rate of collision between particles of size i and j. The first term on the right-hand side of equation (7) describes the creation of particles of size i due to collisions between all possible combinations of particle sizes that sum to i. The term is multiplied by a factor of 1/2 to avoid double counting. The second term describes the destruction of particles of size i due to collisions with particles of any other size j. Equation (7) can be used to write an analogous expression to describe the evolution of the moments of the distribution

$$\frac{\mathrm{d}M_r}{\mathrm{d}t} = \frac{1}{2} \sum_{i=1}^{\infty} \sum_{j=1}^{\infty} \left(i+j\right)^r \beta_{i,j} n_i n_j - \sum_{i=1}^{\infty} \sum_{j=1}^{\infty} i^r \beta_{i,j} n_i n_j \,. \tag{8}$$

The form of the frequency factor $\beta_{i,j}$ depends on the Knudsen number, defined in terms of the mean free path of the gas λ and a representative length scale L

$$\mathrm{Kn} = \frac{2\lambda}{L}\,. \tag{9}$$

The *continuum regime* is characterised by $\mathrm{Kn} \ll 1$ where $\beta_{i,j}$ is given by

$$\beta^{\mathrm{c}}_{i,j} = K_{\mathrm{c}} \left(\frac{C_i}{r_i} + \frac{C_j}{r_j}\right)\left(r_i + r_j\right), \tag{10}$$

where C is the Cunningham slip correction factor

$$C = 1 + 1.257\mathrm{Kn}\,. \tag{11}$$

The *free-molecular regime* is characterised by $\mathrm{Kn} \gg 1$ where $\beta_{i,j}$ is given by

$$\beta^{\mathrm{f}}_{i,j} = \varepsilon_{ij} \sqrt{\frac{8\pi k_{\mathrm{B}} T}{\mu_{i,j}}} \left(r_i + r_j\right)^2, \tag{12}$$

where k_{B} is the Boltzmann constant, T is the temperature, $\mu_{i,j}$ is the reduced mass and r_i is the radius of particles of size i. ε_{ij} is a size-dependent coagulation enhancement factor due to attractive or repulsive inter-particle forces.

In the case of *spherical particles*, equations (10) and (12) may be rewritten

$$\beta^{\mathrm{c}}_{i,j} = K_{\mathrm{c}} \left(\frac{1}{i^{1/3}} + \frac{1}{j^{1/3}} + K_{\mathrm{c}}{}' \left[\frac{1}{i^{2/3}} + \frac{1}{j^{2/3}}\right]\right)\left(i^{1/3} + j^{1/3}\right), \tag{13}$$

$$\beta^{\mathrm{f}}_{i,j} = K_{\mathrm{f}} \left(\frac{1}{i} + \frac{1}{j}\right)^{1/2} \left(i^{1/3} + j^{1/3}\right)^2, \tag{14}$$

with

$$K_{\mathrm{c}} = \frac{2k_{\mathrm{B}}T}{3\mu}, \quad K_{\mathrm{c}}{}' = 2.514\lambda\left(\frac{\pi\rho_{\mathrm{s}}}{6m_1}\right)^{1/3}, \quad K_{\mathrm{f}} = \varepsilon_{ij}\left(\frac{3m_1}{4\pi\rho_{\mathrm{s}}}\right)^{1/6}\left(\frac{6k_{\mathrm{B}}T}{\rho_{\mathrm{s}}}\right)^{1/2}, \tag{15}$$

where μ is the absolute viscosity of the gas. The length scale required by the Knudsen number in equation (11) is specified as the particle diameter d_i. We follow Balthasar [4] and set $\varepsilon_{ij} = 2.2$ for collisions of uncharged particles.

The following sections use the population balance equation (8) to derive rate equations for particle inception, surface growth and coagulation. The resulting surface growth (22) and coagulation equations (25) and (26) require fractional-order moments. The equations are closed by estimating the fractional-order moments using logarithmic Lagrange interpolation between the whole-order reduced moments $\mu_r = M_r/M_0$. This is equivalent to assuming a monodisperse distribution in the two-moment case, $r = 0, 1$.

Inception rate Inception is assumed to occur in the free molecular regime. Equation (8) can be formulated for particle inception by omitting the second term and substituting $\beta_{i,j}^{\mathrm{f}}$ defined in equation (12). In terms of the reaction scheme given by equation (1)

$$\dot{M}_r^{\mathrm{in}} = \frac{1}{2}\sqrt{8\pi k_{\mathrm{B}} T} N_{\mathrm{A}}^2 \sum_{\substack{\text{inception} \\ \text{reactions}}} \frac{\varepsilon_{\alpha\beta}}{\sqrt{\mu_{\alpha,\beta}}} \left(x_\alpha + x_\beta\right)^r \left(r_\alpha + r_\beta\right)^2 C_\alpha C_\beta \,, \tag{16}$$

where each inception reaction uniquely defines

$$C_\alpha = C_{\mathrm{Ti}_{x_\alpha}\mathrm{O}_{y_\alpha}\mathrm{Cl}_{z_\alpha}} \,, \quad C_\beta = C_{\mathrm{Ti}_{x_\beta}\mathrm{O}_{y_\beta}\mathrm{Cl}_{z_\beta}} \,, \tag{17}$$

$$r_\alpha = r_\beta = 0.65 \times 10^{-9}\ \mathrm{m} \,, \tag{18}$$

with

$$\varepsilon_{\alpha\beta} = 2.2 \,, \tag{19}$$

$$\frac{1}{\mu_{\alpha,\beta}} = \frac{N_{\mathrm{A}}}{W_{C_{\mathrm{Ti}_{x_\alpha}\mathrm{O}_{y_\alpha}\mathrm{Cl}_{z_\alpha}}}} + \frac{N_{\mathrm{A}}}{W_{C_{\mathrm{Ti}_{x_\beta}\mathrm{O}_{y_\beta}\mathrm{Cl}_{z_\beta}}}} \,. \tag{20}$$

The smallest unit in the population is defined as $\mathrm{TiO_2}$, such that the smallest particle is size is $(x_\alpha + x_\beta) \geq 2$ and M_1/N_{A} is the number of moles of $\mathrm{TiO_2}$ in the population.

Surface growth rate The surface growth rate may be written in terms of the mechanism defined by equation (3) and the population balance equation (8) using

$$\beta_{i,j}^{\mathrm{sg}} = k_{\mathrm{s}} A_i C_{\mathrm{O_2}} \,. \tag{21}$$

Assuming spherical particles

$$\dot{M}_r^{\mathrm{sg}} = \begin{cases} 0 \,, & r = 0 \\ k_{\mathrm{s}} A_1 C_{\mathrm{O_2}} C_{\mathrm{TiCl_4}} N_{\mathrm{A}} \displaystyle\sum_{k=0}^{r-1} \binom{r}{k} 1^{r-k} \mu_{k+\frac{2}{3}} \, M_0 \,, & r \geq 1 \,, \end{cases} \tag{22}$$

where

$$A_i = A_1 \, i^{2/3} \,, \quad A_1 = 4.787 \times 10^{-19}\ \mathrm{m}^2 \,. \tag{23}$$

The factor of 1^{r-k} arises from the reaction stoichiometry, where each $\mathrm{TiCl_4}$ reacting as per equation (2) contributes one $\mathrm{TiO_2}$ unit to the population.

Coagulation rate The coagulation rate is calculated as described by Frenklach [19]

$$\dot{M}_r^{\mathrm{cg}} = \frac{\dot{M}_r^{\mathrm{c}} \, \dot{M}_r^{\mathrm{f}}}{\dot{M}_r^{\mathrm{c}} + \dot{M}_r^{\mathrm{f}}} \,, \qquad r = 0, 2, 3, \ldots \tag{24}$$

The *continuum* coagulation rate described by equations (8) and (13) is given

$$\dot{M}_r^{\mathrm{c}} = \begin{cases} -K_{\mathrm{c}}\left(1 + \mu_{\frac{1}{3}}\mu_{-\frac{1}{3}} + K_{\mathrm{c}}{}'\left[\mu_{-\frac{1}{3}} + \mu_{\frac{1}{3}}\mu_{-\frac{2}{3}}\right]\right) M_0^2\,, & r = 0 \\ 0\,, & r = 1 \\ \dfrac{K_{\mathrm{c}}}{2}\displaystyle\sum_{k=1}^{r-1}\binom{r}{k}\Big(\mu_{k+\frac{1}{3}}\mu_{r-k-\frac{1}{3}} + 2\mu_k\mu_{r-k} + \mu_{k-\frac{1}{3}}\mu_{r-k+\frac{1}{3}} & \\ \qquad + K_{\mathrm{c}}{}'\Big[\mu_{k+\frac{1}{3}}\mu_{r-k-\frac{2}{3}} + \mu_k\mu_{r-k-\frac{1}{3}} & r \geq 2\,. \\ \qquad + \mu_{k-\frac{1}{3}}\mu_{r-k} + \mu_{k-\frac{2}{3}}\mu_{r-k+\frac{1}{3}}\Big]\Big) M_0^2\,, & \end{cases} \tag{25}$$

The *free molecular* coagulation rate described by equations (8) and (14) is given

$$\dot{M}_r^{\mathrm{f}} = \begin{cases} -\dfrac{1}{2}K_{\mathrm{f}}\left({}^{\frac{1}{2}}f_{0,0}\right) M_0^2\,, & r = 0 \\ 0\,, & r = 1 \\ \dfrac{1}{2}K_{\mathrm{f}}\displaystyle\sum_{k=1}^{r-1}\binom{r}{k}\left({}^{\frac{1}{2}}f_{k,r-k}\right) M_0^2\,, & r \geq 2 \end{cases} \tag{26}$$

with

$${}^{l}f_{x,y} = \sum_{i=1}^{\infty}\sum_{j=1}^{\infty}\frac{i^x j^y}{\sqrt{ij}}\left(i + j\right)^{l}\left(i^{1/3} + j^{1/3}\right)^2 n_i n_j \,/\, M_0^2\,, \qquad l = \frac{1}{2}\,. \tag{27}$$

Equation (27) can only be closed for integer values of l. The function ${}^{\frac{1}{2}}f_{x,y}$ is estimated by logarithmic Lagrange interpolation between evaluations of a grid function

$${}^{m}f_{x,y} = \sum_{k=0}^{m}\binom{m}{k}\Big(\mu_{k+x+\frac{1}{6}}\mu_{m+y-k-\frac{1}{2}} + 2\mu_{k+x-\frac{1}{6}}\mu_{m+y-k-\frac{1}{6}} + \mu_{k+x-\frac{1}{2}}\mu_{m+y-k+\frac{1}{6}}\Big)\,, \qquad m \in \mathbb{N}_{\cdot} \tag{28}$$

using the parameterisation

$$\begin{aligned} m &= 0, \ldots, n-1\,, \\ n &= \min\left(4,\, U - \max(x, y)\right)\,, \qquad U = 3, \ldots, 6\,, \end{aligned} \tag{29}$$

where U is the number of moments in the truncated set such that $r = 0, \ldots, U-1$. This is a generalisation of the method recommended by Frenklach [19] for the case $r = 0, \ldots, 5$.

The following physical properties are assumed

$$m_1 = 1.327 \times 10^{-25}\ \text{kg}\,, \quad \rho_\text{s} = 4260\ \text{kg/m}^3\,, \tag{30}$$

and the mean free path and viscosity are approximated as those of air (T in K, p in Pa)

$$\lambda = 2.370 \times 10^{-5}\,\frac{T}{p}\ \text{m}\,, \tag{31}$$

$$\mu = 1.458 \times 10^{-6}\,\frac{T\sqrt{T}}{T + 100.4}\ \text{kg/ms}\,. \tag{32}$$

2.3 Projected fields method

The PF method uses a weighted field approximation to solve a joint composition PDF transport equation. A projection method is used to derive transport equations that force the statistics of the fields to obey specified moments of the PDF transport equation. The approach was first suggested by Fox [18] under the name DQMoM-IEM (the Direct Quadrature Method of Moments using the Interaction by Exchange with the Mean micromixing model) and its derivation is well documented in the literature. Its implementation and performance as a turbulent reaction closure have been investigated in detail [1, 2].

2.3.1 Terminology

There is a lack of consistency regarding the terminology applied to DQMoM-IEM in the turbulent reacting flow literature. The name QMoM originates from the application of a weighted particle quadrature approximation to close integral terms in a population balance moment equation [36]. The *direct* prefix denotes the case where the method transports the parameters of the approximation, rather than the moments of the population [35]. In the case of turbulent reacting flows, the method is applied to a PDF transport equation that includes the IEM mixing submodel. The suffix was added when the projection was simplified to improve the numerical behaviour of the method [18] and we talk about fields rather than particles because the approximation is continuous in physical space. Since the PDF transport equation contains no integral terms, the quadrature terminology is no longer appropriate. However, the DQMoM-IEM label is often still used (ourselves included). An alternative name, the multi-environment probability density function (MEPDF) method is sometimes applied [14, 67]. This reflects a physical interpretation of the method as a multi-environment reaction model [18, 71], but provides little description of the numerical method. For example, the stochastic fields (SF) method invokes an analogous field approximation to the PDF transport equation [see 2] without the projection and could equally be described as an MEPDF method.

We want to emphasise the distinction between the *model* and the *numerical method*. We consider the PDF transport equation to be the model and the weighted field approximation and projection to be the numerical method. For this reason, we refer to a ***projected fields* (PF) method**. This highlights the projection that distinguishes it from a wider class of mathematically related field methods. It is consistent with the existing SF terminology and is what we adopt in this paper.

2.3.2 Model equations

This paper considers the case when a closed [see 18] Favre-averaged joint composition PDF transport equation

$$\begin{aligned}\langle\rho\rangle\,\frac{\partial\tilde{f}_\phi}{\partial t}+\langle\rho\rangle\,\tilde{U}_i\frac{\partial\tilde{f}_\phi}{\partial x_i}-\frac{\partial}{\partial x_i}\left(\Gamma_{\mathrm{T}}\frac{\partial\tilde{f}_\phi}{\partial x_i}\right)=\\ -\frac{\partial}{\partial\psi_\alpha}\left(\left[\frac{C_\phi}{2\tau_\phi}\big(\langle\phi_\alpha\rangle-\psi_\alpha\big)+S_\alpha\big(\psi\big)\right]\langle\rho\rangle\,\tilde{f}_\phi\right),\end{aligned} \tag{33}$$

is approximated using

$$\begin{aligned}\tilde{f}_\phi\big(\psi(x,t)\big)\;\mathrm{d}\psi&=\tilde{f}_\phi\big(\psi_1,\ldots,\psi_K(x,t)\big)\;\mathrm{d}\psi_1\cdots\mathrm{d}\psi_K\\ &\approx\sum_{n=1}^{N}w^{(n)}(x,t)\prod_{\alpha=1}^{K}\delta_{\psi_\alpha^{(n)}(x,t)}\,\mathrm{d}\psi_\alpha\,,\end{aligned} \tag{34}$$

where

$$\delta_{\psi_\alpha^{(n)}(x,t)}\equiv\delta\big[\psi_\alpha-\psi_\alpha^{(n)}(x,t)\,\big]\,. \tag{35}$$

The approximation introduces N weights $w^{(n)}$ and NK scalar composition variables $\psi_\alpha^{(n)}$, where $\alpha=1,\ldots,K$ scalars.

Transport equations that share the form of standard scalar transport equations are derived

$$\frac{\partial w^{(n)}}{\partial t}+\tilde{U}_i\frac{\partial w^{(n)}}{\partial x_i}-\frac{1}{\langle\rho\rangle}\frac{\partial}{\partial x_i}\left(\Gamma_{\mathrm{T}}\frac{\partial w^{(n)}}{\partial x_i}\right)=a^{(n)}\,, \tag{36}$$

$$\frac{\partial s_\alpha^{(n)}}{\partial t}+\tilde{U}_i\frac{\partial s_\alpha^{(n)}}{\partial x_i}-\frac{1}{\langle\rho\rangle}\frac{\partial}{\partial x_i}\left(\Gamma_{\mathrm{T}}\frac{\partial s_\alpha^{(n)}}{\partial x_i}\right)=b_\alpha^{(n)}\,, \tag{37}$$

where

$$s_\alpha^{(n)}\equiv w^{(n)}\psi_\alpha^{(n)}\,. \tag{38}$$

The source terms $a^{(n)}$ are set to zero and a set of $M=NK$ unmixed empirical moments of the form

$$\big\langle\phi_\alpha^{m_{\lambda\alpha}}\big\rangle_N=\sum_{n=1}^{N}w^{(n)}{\psi_\alpha^{(n)}}^{m_{\lambda\alpha}}\,, \tag{39}$$

are used to derive a linear system of NK equations for the source terms $b_\alpha^{(n)}$. In the case that the moments in equation (39) are specified

$$m_{\lambda\alpha}=\lambda\quad\text{ for }\lambda=1,\ldots,N\text{ and }\alpha=1,\ldots,K\,, \tag{40}$$

the linear system can be solved to give a set of N equations for each scalar $\alpha = 1, \ldots, K$ [1]

$$b_\alpha^{(n)} = b_{\mathrm{mx}_\alpha}^{(n)} + b_{\mathrm{rx}_\alpha}^{(n)} + b_{\mathrm{dx}_\alpha}^{(n)}\,, \tag{41}$$

where

$$b_{\mathrm{mx}_\alpha}^{(n)} = w^{(n)} \frac{C_\phi}{2\tau_\phi} \left(\langle \phi_\alpha \rangle_N - \psi_\alpha^{(n)} \right), \tag{42}$$

$$b_{\mathrm{rx}_\alpha}^{(n)} = w^{(n)} S_\alpha \left(\psi^{(n)} \right), \tag{43}$$

$$\begin{aligned} b_{\mathrm{dx}_\alpha}^{(n)} = {} & w^{(n)} c_{\alpha\alpha}^{(n)} \sum_{\substack{i=1 \\ i \neq n}}^{N} \frac{1}{\psi_\alpha^{(n)} - \psi_\alpha^{(i)}} \\ & + \prod_{\substack{i=1 \\ i \neq n}}^{N} \frac{1}{\psi_\alpha^{(n)} - \psi_\alpha^{(i)}} \sum_{\substack{j=1 \\ j \neq n}}^{N} w^{(j)} c_{\alpha\alpha}^{(j)} \prod_{\substack{k=1 \\ k \neq j,n}}^{N} \left(\psi_\alpha^{(j)} - \psi_\alpha^{(k)} \right), \end{aligned} \tag{44}$$

and

$$c_{\alpha\beta}^{(n)} \equiv \frac{\Gamma_\mathrm{T}}{\langle \rho \rangle} \frac{\partial \psi_\alpha^{(n)}}{\partial x_i} \frac{\partial \psi_\beta^{(n)}}{\partial x_i}\,. \tag{45}$$

The $b_{\mathrm{mx}_\alpha}^{(n)}$ and $b_{\mathrm{rx}_\alpha}^{(n)}$ terms describe micromixing and chemical reaction, $b_{\mathrm{dx}_\alpha}^{(n)}$ describes the effect of turbulent diffusion in the presence of spatial gradients of scalar α. Equation (44) is poorly conditioned and is singular if any $\psi_\alpha^{(n)}$ are equal. Its numerical treatment has been investigated in detail [1].

3 Numerical treatment and coupling

The commercial Star-CD CFD code [8] is used to solve the Favre-averaged Navier-Stokes equations as a transient problem with a k-ε High Reynolds Number turbulence model and standard wall functions. The default model constants were used with unit Prandtl and Schmidt numbers. The PF model is coupled to Star-CD using an operator splitting technique where $w^{(n)}$ and $s_\alpha^{(n)}$ are transported as passive scalars [1]. Changes in composition and temperature are coupled to Star-CD via the density and viscosity using a weak pressure coupling. The method is summarised below.

Equation (37) is solved using a Strang [66] splitting

$$\frac{\partial s_\alpha^{(n)}}{\partial t} = -\tilde{U}_i \frac{\partial s_\alpha^{(n)}}{\partial x_i} + \frac{1}{\langle \rho \rangle} \frac{\partial}{\partial x_i} \left(\Gamma_\mathrm{T} \frac{\partial s_\alpha^{(n)}}{\partial x_i} \right), \tag{46}$$

$$\frac{\partial s_\alpha^{(n)}}{\partial t} = b_\alpha^{(n)} = b_{\mathrm{mx}_\alpha}^{(n)} + b_{\mathrm{rx}_\alpha}^{(n)} + b_{\mathrm{dx}_\alpha}^{(n)}\,, \tag{47}$$

where the source terms $b_\alpha^{(n)}$ are supplied using equations (42–44), equations (36) and (46) are solved using Star-CD with time step Δt, and equation (47) is solved with time step $\frac{1}{2}\Delta t$ before the first and after the last iteration, and time step Δt otherwise. The numerical treatment of equation (47) requires special care. It is solved using the *analytic* solver described by Akroyd et al. [1] such that the current study is limited to $N = 2$ fields. The implementation in this paper invokes a further splitting [2]

$$S_{\Delta t}^{b_\alpha^{(n)}}\left(s_\alpha^{(n)}\right) \approx \left[S_{\frac{1}{2}\Delta t}^{b_{\mathrm{mx}\alpha}^{(n)}} \circ S_{\frac{1}{2}\Delta t}^{b_{\mathrm{dx}\alpha}^{(n)}} \circ S_{\Delta t}^{b_{\mathrm{rx}\alpha}^{(n)}} \circ S_{\frac{1}{2}\Delta t}^{b_{\mathrm{dx}\alpha}^{(n)}} \circ S_{\frac{1}{2}\Delta t}^{b_{\mathrm{mx}\alpha}^{(n)}}\right]\left(s_\alpha^{(n)}\right), \tag{48}$$

where $S_{\Delta t}$ denotes the solution operator

$$S_{\Delta t}^{b_\alpha^{(n)}}\left(s_\alpha^{(n)}\right) \;:\; s_\alpha^{(n)}(t) \mapsto s_\alpha^{(n)}(t+\Delta t)\;.$$

The composition space is defined

$$\phi_\alpha = \begin{cases} Y_\alpha\,, & \alpha = 1,\ldots,s\,, \\ M_r \,/\, \langle\rho\rangle\;, & \alpha = 1+s+r\,, \quad r = 0,\ldots,U-1\,, \\ h\,, & \alpha = 1+s+U = K\,, \end{cases} \tag{49}$$

where Y_α are the species mass fractions, $M_r/\langle\rho\rangle$ are the number moments per unit mass and h is the specific enthalpy. The global bounds required by the method are specified

$$\left[Y_{\mathrm{glb}},\, Y_{\mathrm{gub}}\right] = \left[0,\, 1\right], \tag{50}$$

$$\left[M_{\mathrm{glb}},\, M_{\mathrm{gub}}\right] = \left[0,\, \infty\right], \tag{51}$$

$$\left[h_{\mathrm{glb}},\, h_{\mathrm{gub}}\right] = \left[h\left(T_{\mathrm{glb}}, Y^{(n)}(x,t)\right),\, h\left(T_{\mathrm{gub}}, Y^{(n)}(x,t)\right)\right]. \tag{52}$$

The enthalpy bounds are calculated at the global temperature bounds and the prevailing composition. The temperature bounds are defined using the bounds that accompany the thermodynamic data supplied with the gas-phase mechanism [77].

The micromixing parameters C_ϕ, τ_ϕ and turbulent diffusivity Γ_{T} required by the micromixing and diffusion terms in equation (48) are calculated

$$C_\phi = 2.0\,, \tag{53}$$

$$\tau_\phi = k/\varepsilon\,, \tag{54}$$

$$\Gamma_{\mathrm{T}} = \nu_{\mathrm{T}}/\sigma_{\mathrm{T}}\,, \tag{55}$$

where k, ε and ν_{T} are the turbulent kinetic energy, turbulent dissipation and turbulent viscosity prescribed by Star-CD and $\sigma_{\mathrm{T}} = 0.7$.

The reaction solution operator in equation (48) is implemented using RADAU5 [27] to numerically integrate the reaction term in equation (47). The reaction system is solved in terms of the molar concentrations $C_\alpha^{(n)}$, the number moments per unit volume $M_r^{(n)}$ and the temperature $T^{(n)}$ of each field. The source terms are written

$$S_\alpha\left(\begin{bmatrix} C_\alpha^{(n)} \\ M_r^{(n)} \\ T^{(n)} \end{bmatrix}\right) = \begin{bmatrix} \dot{C}_\alpha^{(n)} \\ \dot{M}_r^{(n)} \\ \dot{T}^{(n)} \end{bmatrix},$$

where the total moment source terms are given

$$\dot{M}_r^{(n)} = \dot{M}_r^{(n)^{\text{in}}} + \dot{M}_r^{(n)^{\text{sg}}} + \dot{M}_r^{(n)^{\text{cg}}} \,, \tag{56}$$

with $\dot{M}_r^{(n)^{\text{in}}}$, $\dot{M}_r^{(n)^{\text{sg}}}$ and $\dot{M}_r^{(n)^{\text{cg}}}$ defined as per equations (16), (22) and (24). The concentration source terms due to gas-phase reaction are calculated using the mechanism of West et al. [77]. The additional contributions due to particle formation are calculated

$$\dot{C}_\alpha^{(n)} = \sum_i \frac{\nu_{\alpha i}}{\nu_{\text{TiO}_2 i}} \frac{\dot{M}_{1i}^{(n)}}{N_\text{A}} \,, \tag{57}$$

where the sum is over the set of inception and surface reactions, $\nu_{\alpha i}$ is the stoichiometric coefficient of species α in reaction i, and $\dot{M}_{1i}^{(n)}$ is the contribution to $\dot{M}_1^{(n)}$ due to reaction i. The gas-phase and particles are assumed to have the same temperature T, where the source term due to all reactions (gas-phase, inception and surface growth) is given

$$\dot{T}^{(n)} = -\frac{\sum_{\alpha=1}^{s} h_\alpha^{(n)} \, \dot{C}_\alpha^{(n)} \, W_\alpha}{\sum_{\alpha=1}^{s} c_{\text{p}_\alpha} C_\alpha^{(n)} W_\alpha} \,. \tag{58}$$

The total source terms are adjusted to account for the rate of gas-phase expansion γ

$$\dot{C}_\alpha^{(n)} \leftarrow \dot{C}_\alpha^{(n)} - \gamma^{(n)} \, C_\alpha^{(n)} \,, \quad \dot{M}_r^{(n)} \leftarrow \dot{M}_r^{(n)} - \gamma^{(n)} \, M_r^{(n)} \,, \tag{59}$$

where $\gamma^{(n)}$ is calculated using the ideal gas law at constant pressure

$$pV\big(1 - f_\text{v}\big) = nRT \,, \tag{60}$$

$$\gamma = \frac{\dot{V}}{V} \,, \quad \gamma^{(n)} = \frac{\dot{f}_\text{v}^{\,(n)}}{1 - f_\text{v}^{(n)}} + \frac{\dot{T}^{(n)}}{T^{(n)}} + \frac{\sum_{\alpha=1}^{s} \dot{C}_\alpha^{(n)}}{\sum_{\alpha=1}^{s} C_\alpha^{(n)}} \,, \tag{61}$$

where $V\big(1 - f_\text{v}\big)$ is gas-phase volume and $f_\text{v}^{(n)}$ is calculated as per equation (6)

$$f_\text{v}^{(n)} = \frac{m_1}{\rho_\text{s}} M_1^{(n)} \,, \quad \dot{f}_\text{v}^{\,(n)} = \frac{m_1}{\rho_\text{s}} \dot{M}_1^{(n)} \,. \tag{62}$$

An updated density and viscosity are passed to Star-CD after each time step

$$\langle \rho \rangle = \langle \rho_\text{g} \rangle + \langle \rho_\text{s} \rangle \,, \tag{63}$$

where ρ_g is a gas-phase density estimated using the ideal gas law in equation (60)

$$\langle \rho_\text{g} \rangle = \frac{p\big(1 - \langle f_\text{v} \rangle_N\big)}{R \, \langle T \rangle_N \sum_{\alpha=1}^{s} \frac{\langle Y_{\text{g}\,\alpha} \rangle_N}{W_\alpha}} \,, \tag{64}$$

Y_g are the gas-phase mass fractions and ρ_s is the solid-phase density

$$\langle \rho_\text{s} \rangle = m_1 \, \langle M_1 \rangle_N \,. \tag{65}$$

The viscosity is calculated using equation (32)

$$\langle \mu \rangle = 1.458 \times 10^{-6} \, \frac{\langle T \rangle_N \sqrt{\langle T \rangle_N}}{\langle T \rangle_N + 100.4} \; \text{kg/ms} \,. \tag{66}$$

4 Numerical experiments and validation

This section investigates the performance of the PF method for a model problem involving strong two-way coupling between detailed gas-phase chemistry and titania nanoparticles undergoing simultaneous inception, coagulation and surface growth.

Section 4.1 introduces salient details of the model problem. Section 4.2 considers some ideal reactor cases. It checks the MoMIC implementation and compares results to experimental data. Section 4.3 validates the PF implementation in a scalar mixing case. Section 4.4 demonstrates the application of the method to the full reacting case.

4.1 Model problem

The investigations is this paper consider the production of titania nanoparticles in a lab scale 'slot' reactor. The geometry and input conditions are representative of industrial conditions for the chloride process. The reactor configuration is illustrated in **figure 1**.

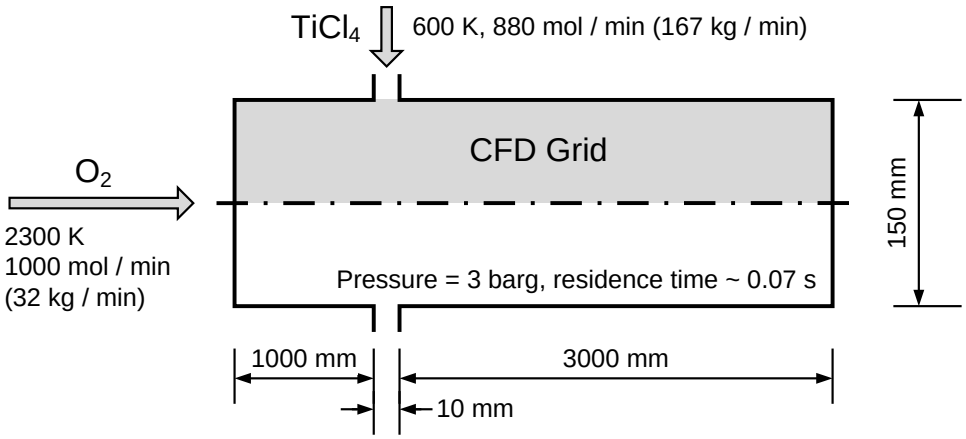

Figure 1: *Configuration of the titania reactor.*

The reactor is modelled using a wedge-shaped domain with boundary conditions to exploit axial symmetry. Star-CD [8] was used to solve the Favre-averaged Navier-Stokes and PF equations as per section 3. The initial and inlet boundary conditions are given in **table 1**. The turbulence boundary conditions were estimated using empirical correlations

$$l = 0.07L\,, \quad \mathrm{TI} = 0.16\mathrm{Re}_{D_\mathrm{H}}^{(-1/8)}\,, \tag{67}$$

where l is the mixing length and TI is the turbulence intensity. L is a length scale and $\mathrm{Re}_{D_\mathrm{H}}$ a Reynolds number, both based on the relevant hydraulic diameter.

Two grids were considered. The first is a *base* grid. It uses a 238×15 (axial×radial) domain of fully structured hexahedral cells. The axial cell spacing is shrunk into and stretched out of the reaction zone by a factor of 1.05 subject to the size bounds [5, 50] mm. The second is a *refined* version of the base grid. It uses a 588×30 (axial × radial) domain subject to the same axial stretching and size bounds [2.5, 25] mm. All cases were solved with time step 2×10^{-5} s on the base grid and 6×10^{-6} s on the refined grid.

Table 1: *Titania reactor initial and inlet boundary conditions.*

	Initial condition	Inlet boundary		
		Axial inlet	Radial inlet	
$w^{(n)}$	$1/N$	0	1	for $n = 1$
	$1/N$	1	0	for $n = 2$
$Y^{(n)}_{\mathrm{TiCl_4}}$	1	0	1	
$Y^{(n)}_{\mathrm{O_2}}$	0	1	0	
$Y^{(n)}_{\alpha}$	0	0	0	for $\alpha \neq \mathrm{TiCl_4}, \mathrm{O_2}$
$M^{(n)}_r / \langle\rho\rangle$	0	0	$4^r \times 10^{10}$	for section 4.3
	0	0	0	for section 4.4
$T^{(n)}$	600	2300	600	
$\langle\rho\rangle$	–	0.669	15.2	kg/m^3
$\langle\mu\rangle$	–	6.7×10^{-5}	3.1×10^{-5}	kg/ms
Volumetric flow	–	0.797	0.183	m^3/s
Mixing length	–	0.011	0.001	m
Turbulence intensity	–	0.038	0.034	-

Note that the table specifies the scalars in terms of Y_α, M_r and T, but that the PF method transports $w^{(n)}$ and $s^{(n)}_\alpha = w^{(n)}\psi^{(n)}_\alpha$, where the composition space is defined by equation (49) and $h^{(n)}$ is calculated $h^{(n)} = h\left(T^{(n)}, Y^{(n)}\right)$.

4.2 Ideal reactor studies

This section considers some ideal reactor cases. It checks that MoMIC has been correctly implemented and reproduces experimental data. The simulations are performed by solving equation (47) for the $N = 1$ case. This is equivalent to assuming perfect mixing. It gives insight into the behaviour of the reaction without spatial transport and in isolation from the micromixing and diffusion terms described in section 2.3.

Figure 2 validates the MoMIC implementation against test data from an established stochastic population balance model [24, 43, 44, 73]. The initial conditions were defined as a binary mixture of 100:88 (mol/mol) $\mathrm{O_2} : \mathrm{TiCl_4}$ at 3 barg based on figure 4.1. Both methods were solved under isothermal conditions at 2100 K and 1500 K (not shown) using the chemical mechanism described in section 2.1 with a spherical particle model. The test data were generated using both a predictor-corrector coupling to the gas-phase chemistry [11] and by post processing the gas-phase data from the MoMIC simulations.

MoMIC shows excellent agreement with the test data for the concentrations of key gas-phase species and the zeroth and first moments of the titania particle number distribution.

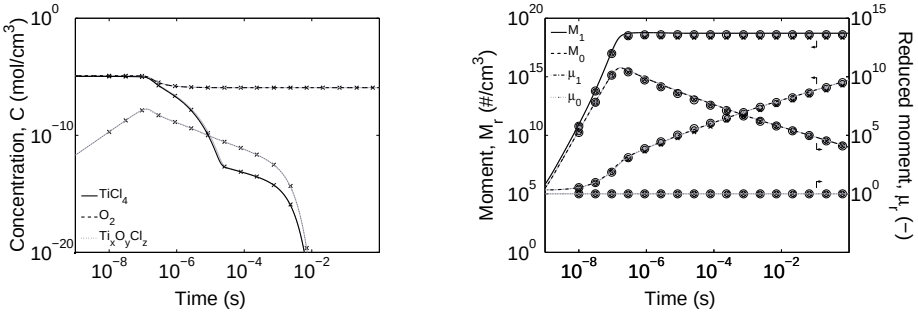

(a) *Gas-phase concentrations.* **(b)** *Particle number moments.*

Figure 2: *Titania batch reactor concentration and particle number moments at $T = 2100$ K. Black lines: MoMIC, $U = 3$; Gray lines: MoMIC, $U = 6$; Open symbols: Test data, predictor-corrector splitting and 256 (×) stochastic particles; Closed symbols: Test data, gas-phase data post-processed with 256 (○) and 4096 (●) stochastic particles.*

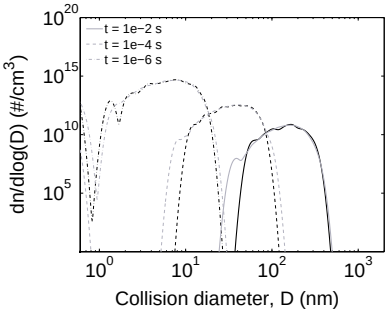

Figure 3: *Titania batch reactor particle number distributions calculated from Figure 2(b). Black lines: 256 stochastic particles; Gray lines: 4096 stochastic particles.*

The oxygen is in slight excess and is not completely consumed. The rapid consumption of the titanium species is dominated by surface reaction. This is consistent with industrial experience of the chloride process. The test data show that the particle number moments can be accurately reproduced by post-processing the gas-phase composition with as few as 256 stochastic particles. The MoMIC data show little sensitivity to an increase from $U = 3$ to $U = 6$ moments. All remaining MoMIC simulations in this paper set $U = 3$.

Figure 3 shows particle number distributions calculated using the stochastic population balance model to post-process the gas-phase data in figure 2(a). The data show the emergence of a bimodal distribution due to coagulation, with mean particle size approximately 200 μm after 0.01 s. There is reasonable agreement between the 256 and 4096 stochastic particle cases, but with more pronounced differences than are apparent in figure 2(b).

Figure 4 shows non-isothermal MoMIC simulations with different initial temperatures. Figure 4(a) shows an initial endothermic induction period due to decomposition of $TiCl_4$, followed by a rapid exotherm as the reaction 'takes off'. Higher initial temperatures give shorter inductions times. The final temperatures are in the range 1850–2200 K and are determined by the initial temperature and gas-phase equilibria. The initial temperature of 1082 K is that given by the inlet streams in figure 1 if they are allowed to mix without

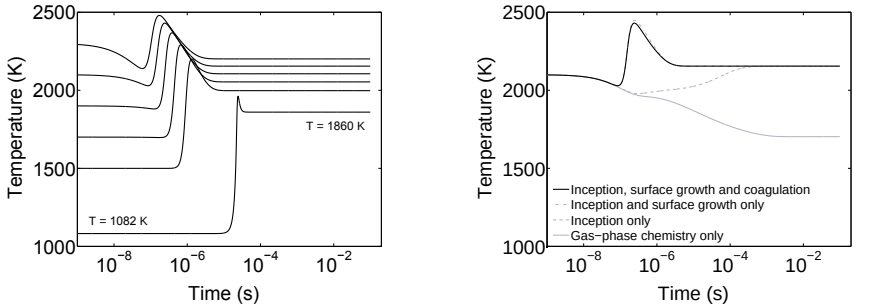

(a) *Effect of initial temperature.* **(b)** *Effect of the particle processes.*

Figure 4: *Titania batch reactor non-isothermal temperature profiles.*

reacting and corresponds to a final temperature of 1860 K. Figure 4(b) shows temperature profiles in the absence of the MoMIC inception, surface growth and coagulation processes for an initial temperature of 2100 K. The exotherm is mainly caused by surface growth and is slightly moderated by the reduction in surface area due to coagulation.

Figure 5 shows good agreement between MoMIC and experimental data from Pratsinis et al. [50]. The original investigation measured the reaction of 5:1 (mol/mol) O_2 : $TiCl_4$ in argon (99% by volume) in a 1/8-in-I.D. tube heated to 973–1273 K. Pratsinis et al. [50] estimate an effective rate constant for the overall oxidation kinetics of $TiCl_4$ vapour

$$k_{\text{eff}} = -\frac{\ln(C_{\text{o}}/C_{\text{i}})}{t}\,, \tag{68}$$

assuming the reaction is first-order in $TiCl_4$ with Arrhenius kinetics and where C_{i} and C_{o} are the measured inlet and outlet $TiCl_4$ concentrations and t is residence time in the isothermal zone of the reactor held at temperature T. This experiment was modelled using an imposed temperature profile taken from Pratsinis et al. [50, Fig. 3]. The data are presented in the original form [50, Fig. 4] for easy comparison.

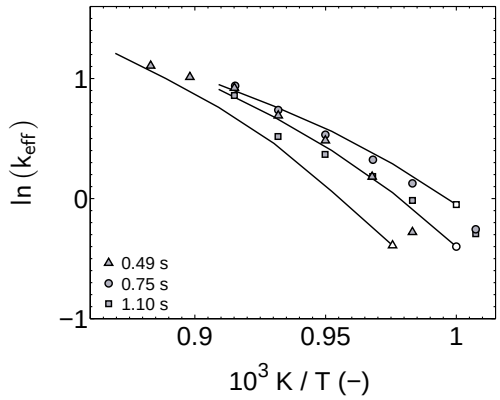

Figure 5: *Arrhenius plot of the oxidation rate of $TiCl_4$ at three different residence times. Black lines with open symbols: MoMIC; Closed symbols: Experimental data [50, Fig. 4].*

4.3 Scalar mixing validation

This section checks the PF implementation in a (non-reacting) scalar mixing case. The boundary conditions in table 1 are used to introduce a monodisperse particle distribution at the $TiCl_4$ inlet to ensure non-zero valued moments. The PF model is assessed against a reference solution provided using the method of moments. The application of the method of moments to such problems is well established and provides an exact solution to equation (33) where the chemical source term is zero, $S_\alpha = 0$. This approach has previously been used to validate the numerical treatment of the mass fractions in the PF code used in this paper [1, 2].

The flow field was solved using the method of moments. We describe it as a 'cold' flow field because it pertains to the non-reacting case. **Figure 6** shows the major features of the velocity field near the $TiCl_4$ inlet. There is a recirculation zone near the wall immediately downstream of the inlet and a large increase in the centreline velocity due to the change in density as cold material from the $TiCl_4$ inlet mixes with hot material in the reactor.

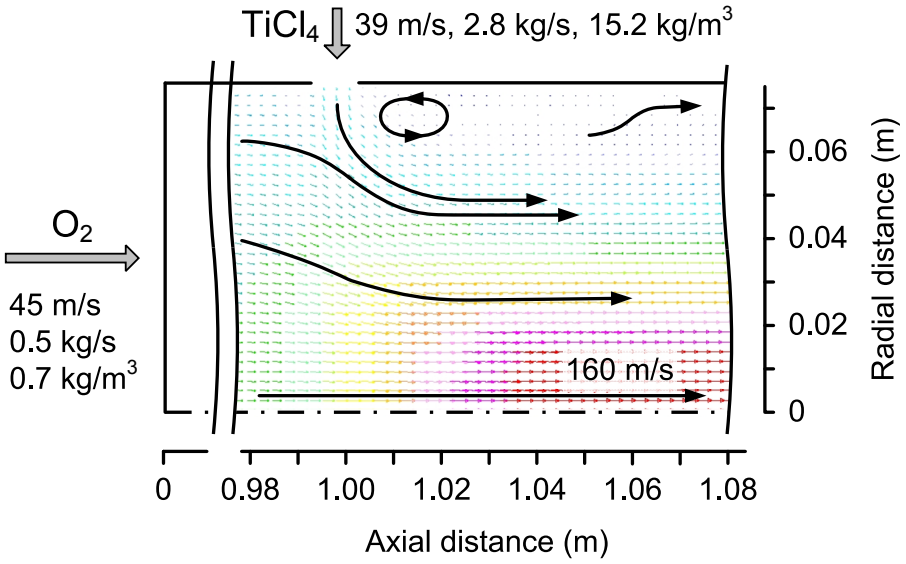

Figure 6: *Titania reactor 'cold' velocity field.*

The remaining simulations in this section are performed without re-solving the flow field. This ensures that any differences between the method of moments and the PF method are due to the numerical implementation of the micromixing and diffusion terms described in section 2.3, as opposed to the subsequent coupling of such differences to the flow field.

Figure 7 presents empirical moments of the enthalpy fields from the PF model on the refined grid for 1 m of reactor downstream of the $TiCl_4$ inlet. Figure 7(a) shows the mean enthalpy. The mean mass fraction and number moment per unit mass fields share the same topology, with values scaled by the corresponding inlet boundary conditions. Figure 7(b) shows the standard deviation of the enthalpy. Again, the standard deviation of the mass fractions and number moments per unit mass share the same topology, but scaled by the difference between the corresponding inlet boundary values. The 'plume' from the $TiCl_4$ inlet marks the mixing zone in the reactor.

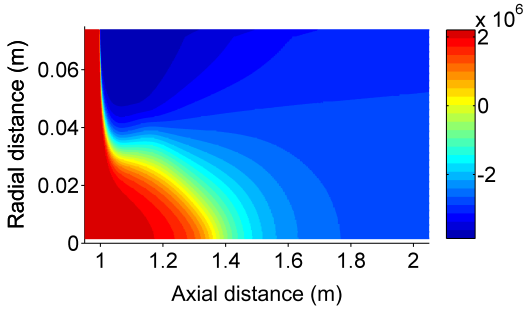

(a) *Mean enthalpy* $\langle h \rangle_{N=2}$ *(J/kg).*

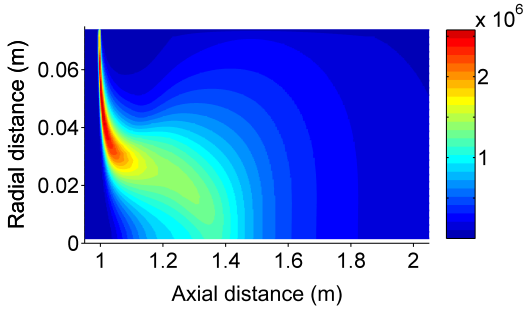

(b) *Enthalpy standard deviation* $\sqrt{\langle h'^2 \rangle}_{N=2}$ *(J/kg).*

Figure 7: *Titania reactor empirical moments of enthalpy for the inert case.*

Table 2 shows convergence data to validate the PF implementation against the method of moments reference solution. The convergence was assessed using the metrics

$$\epsilon_{\text{mean}} = \epsilon\left(\langle \phi_\alpha \rangle_N \,, \quad \langle \phi_\alpha \rangle_{\text{MoM}} \right), \quad \epsilon_{\text{sd}} = \epsilon\left(\sqrt{\langle \phi'^2_\alpha \rangle}_N, \quad \sqrt{\langle \phi'^2_\alpha \rangle}_{\text{MoM}} \right), \tag{69}$$

where

$$\epsilon(x, y) = \frac{\|x - y\|}{\|x + y\|}, \tag{70}$$

and $\|\cdot\|$ denotes an L^2-norm over space. The variances are defined

$$\left\langle \phi'^2_\alpha \right\rangle_N = \left\langle \phi^2_\alpha \right\rangle_N - \langle \phi_\alpha \rangle^2_N, \tag{71}$$

and likewise for the method of moments. The means are in excellent agreement. The standard deviations are in good agreement and show the same value of ϵ_{sd} for all scalars on a given grid. The data show some minor grid dependence, but are sufficient to demonstrate equivalent numerical treatment of the enthalpy and number moments per unit mass versus that previously validated for the mass fractions [1, 2]. Note that the values of ϵ_{sd} differ from previously [1, 2] because the metric in equation (70) is normalised to allow direct comparison between all scalars, regardless of their magnitudes.

Table 2: *Convergence of the PF empirical mean and standard deviation versus the method of moments for the inert titania reactor case.*

Grid	ϵ_{mean}	ϵ_{sd}
	$\phi_\alpha^\top = \left[Y_1 \cdots Y_s \ \frac{M_0}{\langle\rho\rangle} \cdots \frac{M_2}{\langle\rho\rangle} \ h\right]$	$\phi_\alpha^\top = \left[Y_1 \cdots Y_s \ \frac{M_0}{\langle\rho\rangle} \cdots \frac{M_2}{\langle\rho\rangle} \ h\right]$
Base	$< 10^{-8}$	1.2×10^{-2}
Refined	$< 10^{-8}$	7.8×10^{-3}

Figure 8 presents temperature data corresponding to figure 7. Figure 8(a) shows the mean temperature field and an outlet temperature of 1082 K consistent with figure 4(a).

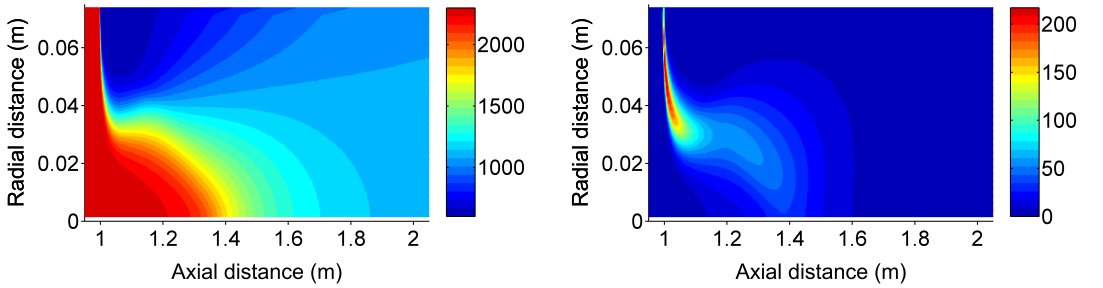

(a) *Mean temperature* $\langle T \rangle_{N=2}$ *(K).* **(b)** *Temperature difference* $\langle T \rangle_{MoM} - \langle T \rangle_{N=2}$ *(K).*

Figure 8: *Titania reactor empirical moments of temperature for the inert case.*

The mean temperature is a non-linear function of the mass fractions and enthalpy, so looks slightly different from figure 7(a). The calculation of the mean temperature is closed by the PF method, but unclosed in the method of moments. The method of moments case estimates an approximate temperature from the mean mass fractions and enthalpy. The effect of this approximation is shown in figure 8(b) and correlates with the location of the standard deviation in figure 7(b). The method of moments case overestimates the temperature in the mixing zone by up to 200 K.

4.4 Titania reactor simulations

This section describes the application of the PF method to simulations of the titania reactor discussed in section 4.1. All simulations were performed on both grids with $U = 3$ moments and include fully coupled solution of the Favre-averaged Navier-Stokes equations, detailed gas-phase chemistry and titania nanoparticles undergoing simultaneous inception, coagulation and surface growth. The figures present data for the refined grid.

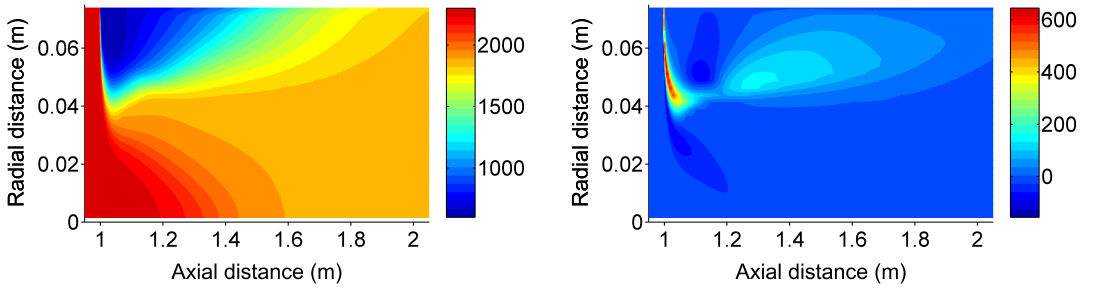

(a) *Mean temperature* $\langle T \rangle_{N=2}$ *(K).* **(b)** *Difference* $\langle T \rangle_{perfect\ mixing} - \langle T \rangle_{N=2}$ *(K).*

Figure 9: *Titania reactor empirical mean temperature for the reacting case.*

Figure 9 shows the mean temperature in the reactor. Comparison of Figures 8(a) and 9(a) shows a significant exotherm due to the reaction. The temperature rise starts in the mix-

ing zone between the inlet streams and extends the length of the reactor downstream, with radial gradients broadening due to mixing. The outlet temperature is 1860 K and is consistent with figure 4(a). Figure 9(b) shows the difference in mean temperature from a perfect mixing case that solves the PF equations for the $N=1$ case. This is equivalent to assuming infinitely fast mixing and is a common engineering approximation. The perfect mixing case overestimates the temperature in the mixing zone by up to 600 K.

Figure 10 shows the zeroth and first moments of the particle number density. The zeroth moment corresponds to the total number of particles per unit volume, the first moment is proportional to the total mass of particles per unit volume. Figure 10(a) shows an area of high number density caused by inception at the leading edge of the mixing zone. The inception zone persists downstream in the area corresponding to a mean temperature $1450 \leqslant \langle T \rangle_{N=2} \leqslant 1850$ K. Elsewhere the number density decreases due to coagulation and mixing. Figure 10(c) shows that most mass is added to the population due to surface growth starting just downstream of the inception zone. The region of largest mass is concentrated in the area of higher number density downstream of the $TiCl_4$ inlet. Figures 10(b) and (d) compare the results to the perfect mixing case. The differences are most pronounced in the mixing zone near the $TiCl_4$ inlet and are of the same order of magnitude as the data in Figures 10(a) and (c). The differences decrease downstream due to mixing.

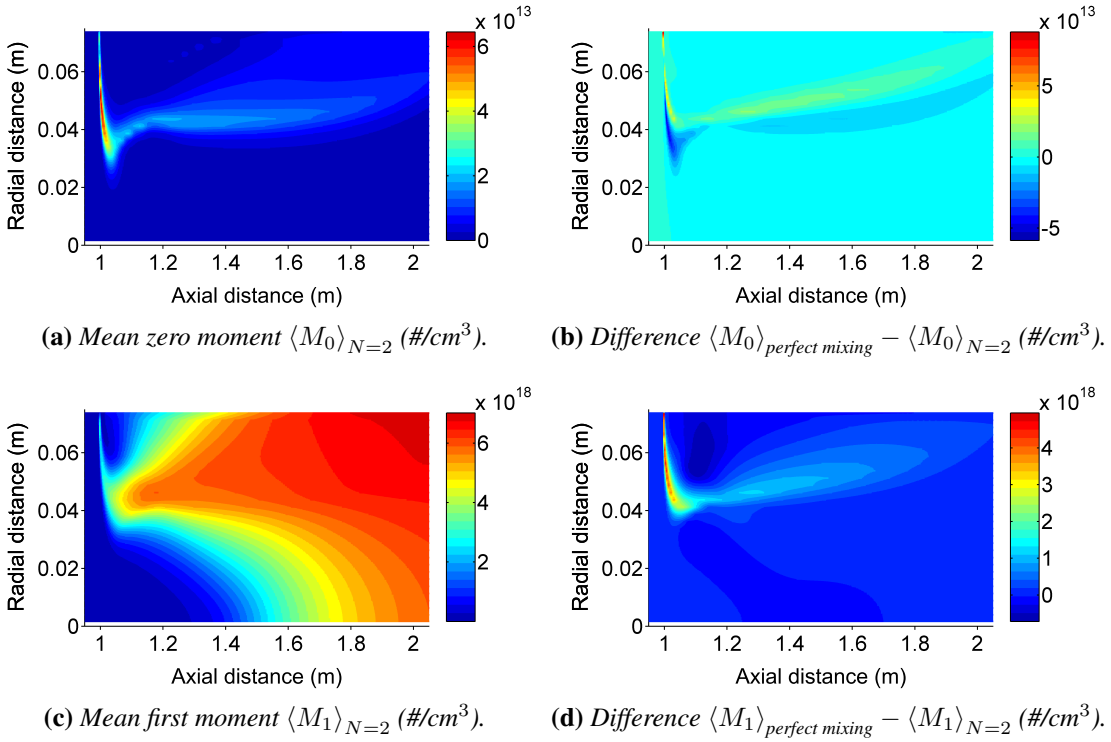

(a) *Mean zero moment* $\langle M_0 \rangle_{N=2}$ *(#/cm*^{3}*).*

(b) *Difference* $\langle M_0 \rangle_{perfect\ mixing} - \langle M_0 \rangle_{N=2}$ *(#/cm*^{3}*).*

(c) *Mean first moment* $\langle M_1 \rangle_{N=2}$ *(#/cm*^{3}*).*

(d) *Difference* $\langle M_1 \rangle_{perfect\ mixing} - \langle M_1 \rangle_{N=2}$ *(#/cm*^{3}*).*

Figure 10: *Titania reactor empirical mean particle number moments for the reacting case.*

Figure 11 shows the mean concentrations of $TiCl_4$ and $Ti_xO_yCl_z$. Figure 11(a) shows that $TiCl_4$ exists in the low-temperature region downstream of the inlet. It decomposes

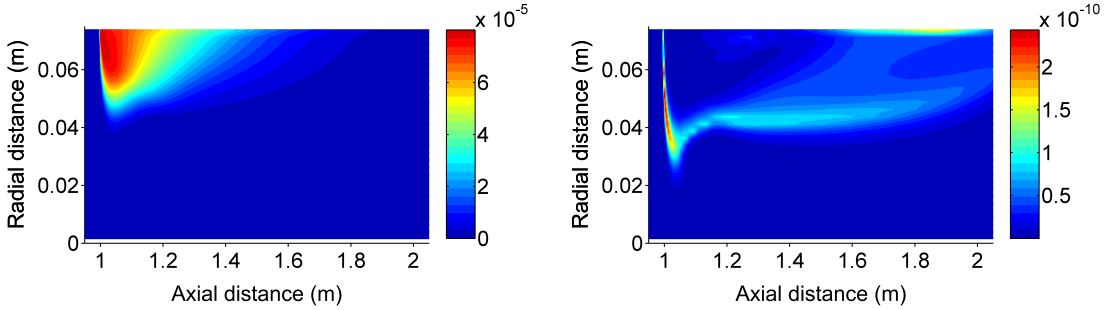

(a) *Mean conc.* $\langle C_{\mathrm{TiCl_4}} \rangle_{N=2}$ *(mol/cm*^{3}*).* **(b)** *Mean conc.* $\langle C_{\mathrm{Ti}_x\mathrm{O}_y\mathrm{Cl}_z} \rangle_{N=2}$ *(mol/cm*^{3}*).*

Figure 11: *Titania reactor empirical mean concentrations for the reacting case.*

via TiCl_z, $z < 4$ and oxidises to form $\mathrm{Ti}_x\mathrm{O}_y\mathrm{Cl}_z$ species as the temperature increases due to mixing with material from the O_2 inlet. Figure 11(b) shows the total concentration of all $\mathrm{Ti}_x\mathrm{O}_y\mathrm{Cl}_z$ species. The inception model in equation (1) specifies $\mathrm{Ti}_x\mathrm{O}_y\mathrm{Cl}_z$ as the incepting species and strong correlation is observed between the concentration in figure 11(b) and the particle number density in figure 10(a).

Figure 12 presents the particle number moments in terms of the particle diameter

$$d = d_1 \mu_{\frac{1}{3}}, \quad \sigma = d_1 \sqrt{\mu_{\frac{2}{3}} - \mu_{\frac{1}{3}}^2}. \tag{72}$$

where d is the mean and σ is the standard deviation of the diameter. Note that these plots show the *full length of the reactor* downstream of the TiCl_4 inlet. The data show lower diameter and standard deviation corresponding to the inception zone in figure 10(a). Elsewhere the diameter increases due to surface growth and coagulation. The standard deviation shows a narrower distribution in the region where figure 10(c) shows most surface growth. This is consistent with previous studies where surface growth is shown to decrease the width of the distribution [49, 68]. These effects diminish downstream due to mixing. In this example, there are effectively no remaining radial gradients at the outlet.

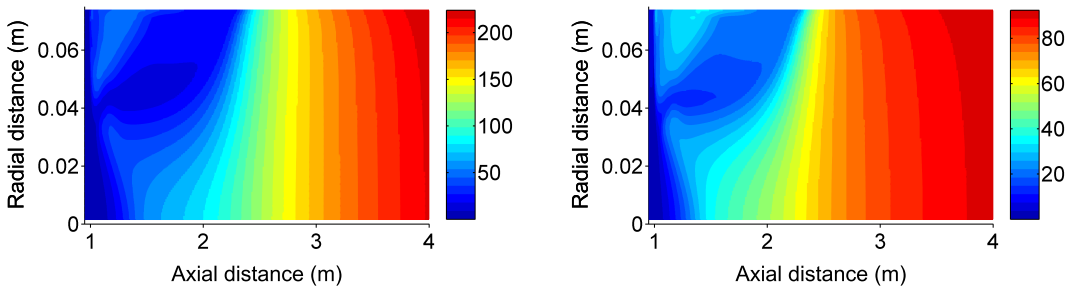

(a) *Mean particle diameter* $\langle d \rangle_{N=2}$ *(nm).* **(b)** *Standard deviation* $\langle \sigma \rangle_{N=2}$ *(nm).*

Figure 12: *Titania reactor empirical moments of the particle size for the reacting case.*

5 Conclusions

This paper has investigated the first part of a two-stage methodology for the detailed modelling of nanoparticle formation in turbulent reacting flows, including detailed chemistry and full coupling between the flow, material and energy balance equations. The paper considers the example of the chloride process for the industrial synthesis of titania nanoparticles in a representative 'slot' reactor geometry.

The objective of the first stage of the methodology is to achieve a reasonable description of the velocity field and gas-phase composition PDF for minimum computational effort. The second stage is to apply a detailed population balance model to investigate the evolution of the nanoparticles without the need to re-solve the chemistry or flow. The objective of the second stage is to allow free choice of the detailed population balance so that it may be chosen to suit the objectives of the study, rather than based on considerations of how to couple it to the simulation of the chemistry and flow.

A projected fields (PF) method has been extended to combine the method of moments with interpolative closure (MoMIC) population balance model and detailed titania chemistry. The PF method is coupled to the Star-CD CFD code using an operator splitting technique. The implementation of MoMIC and the titania chemistry is validated against ideal reactor simulations using an established population balance model and against experimental data. The numerical treatment of the PF method within the CFD code is validated against a reference solution provided using the method of moments for a non-reacting test case. The data show a substantial mixing zone near the reactor inlets, indicated by a region of high standard deviation in mixture enthalpy, particle number moments and mass fractions.

The feasibility of the first stage of the methodology is demonstrated for simulations of titania nanoparticle formation in the 'slot' reactor, including fully coupled solution of the flow, detailed chemistry and particles undergoing simultaneous inception, coagulation and surface growth. The data show significant radial inhomogeneities near the slot. In this example, the inhomogeneities diminish downstream due to mixing. However, designs with multiple inlets would introduce inhomogeneities down the length of the reactor. The predicted temperature and particle properties are compared with a perfect mixing case and show significant differences near the slot. The post processing in the second stage of the methodology will need to consider the full composition PDF, not just the mean composition. The details of how to implement the second stage remain an open question.

Acknowledgements

The authors thank reSolutions Ltd. and the EPSRC (EP/C537564/1) for financial support of Jethro Akroyd, Tioxide Europe Ltd. for financial support of Raphael Shirley and Dr Simon Lo of CD-adapco for licences and technical support.

Nomenclature

Upper-case Roman

A	Surface area per unit volume of the TiO_2 population
A_i	Surface area of particle of size i
C_i	Cunningham slip correction factor for particles of size i
C_α	Molar concentration of species α
C_ϕ	IEM micromixing model constant
D	Collision diameter
D_H	Hydraulic diameter
K	Number of scalars
$K_\mathrm{c},\ K_\mathrm{c}'$	Size-independent parts of $\beta_{i,j}^\mathrm{c}$
K_f	Size-independent part of $\beta_{i,j}^\mathrm{f}$
Kn	Knudsen number
L	Length scale
M	Number of empirical PF moments
M_r	Moment of the number density distribution of order r
N	Number of fields
N_A	Avagadro constant
R	Universal gas constant
Re	Reynolds number
S	Chemical source term
$S_{\Delta t}$	Solution operator for an evolution equation
T	Temperature
U	Number of MoMIC number density moments
$\tilde{U}$	Favre-averaged Eulerian velocity
V	Volume
W_α	Relative molecular mass of species α
Y_α	Mass fraction of species α

Lower-case Roman

$a^{(n)}$	Source term for the weights $w^{(n)}$
$b_\alpha^{(n)}$	Source term for the weighted composition $s_\alpha^{(n)}$
c_p	Specific heat capacity
$c_{\alpha\beta}^{(n)}$	Turbulent diffusion-spatial gradient term for scalars α and β
d	Mean particle diameter
d_i	Diameter of particle of size i
f_v	Particle volume fraction
${}^m f_{x,y}$	Grid function

$\tilde{f}_\phi$ Favre-averaged joint composition PDF of ϕ
h Specific enthalpy
k Turbulent kinetic energy
k_B Boltzmann constant
k_s Rate constant for surface growth reaction
l Mixing length
m_1 Mass of single TiO_2 unit
m_i Mass of particle of size i
$m_{\lambda\alpha}$ Moment order of the λ^{th} empirical PF moment of scalar α
n Number of moles
n Total number density
n_i Number density of particles of size i
p Pressure
r Moment order of the number density moment M_r
r_i Radius of particle of size i
s Number of species
$s_\alpha^{(n)}$ Weighted composition of scalar α
t Time
$w^{(n)}$ Weight
x Position

Upper-case Greek

Γ_T Turbulent diffusivity

Lower-case Greek

$\beta_{i,j}$ Frequency factor for collisions between particles of size i and j
γ Rate of gas-phase expansion
δ Dirac delta function
ϵ_{mean} Convergence metric for the empirical mean
ϵ_{sd} Convergence metric for the empirical standard deviation
ε Turbulent dissipation rate
ε_{ij} Enhancement factor for collisions collisions between particles of size i and j
λ Mean free path
μ Absolute viscosity
$\mu_{i,j}$ Reduced mass of particles of size i and j
μ_r Reduced moment of the population number density, $\mu_r = M_r/M_0$
ν_T Turbulent viscosity
ν_α Stoichiometric coefficient of species α
ρ Density
σ Standard deviation of the particle diameter

σ_{T}	Turbulent Schmidt / Prandtl number
τ_ϕ	IEM micromixing model mixing time
ϕ	Eulerian passive scalar (composition) vector
ψ	Sample space variable corresponding to ϕ
$\psi_\alpha^{(n)}$	Value of scalar α

Superscripts

(n)	Denotes the n^{th} field

Subscripts

c	Denotes the continuum regime
cg	Denotes coagulation
f	Denotes the free molecular regime
g	Denotes the gas-phase
glb	Denotes a global lower bound
gub	Denotes a global upper bound
in	Denotes inception
s	Denotes the solid-phase
sg	Denotes surface growth

Symbols

$\langle \cdot \rangle$	Expectation
$\langle \cdot^2 \rangle$	Expected second moment
$\langle \cdot'^2 \rangle$	Expected variance
$\langle \cdot \rangle_{\text{MoM}}$	Expectation calculated using the method of moments
$\langle \cdot \rangle_N$	Empirical expectation calculated over N fields

Abbreviations

CFD	Computational fluid dynamics
DQMoM	Direct quadrature method of moments
IEM	Interaction by exchange with the mean
MEPDF	Multi-environment probability density function
MoM	Method of moments
MoMIC	Method of moments with interpolative closure
PDF	Probability density function
PF	Projected fields method
QMoM	Quadrature method of moments
SF	Stochastic fields method
TI	Turbulence intensity

References

[1] J. Akroyd, A. Smith, L. R. McGlashan, and M. Kraft. Numerical investigation of DQMoM-IEM as a turbulent reaction closure. *Chemical Engineering Science*, 65 (6):1915–1924, 2010. doi:10.1016/j.ces.2009.11.010.

[2] J. Akroyd, A. Smith, L. R. McGlashan, and M. Kraft. Comparison of the stochastic fields method and DQMoM-IEM as turbulent reaction closures. *Chemical Engineering Science*, 65(20):5429–5441, 2010. doi:10.1016/j.ces.2010.06.039.

[3] J. Appel, H. Bockhorn, and M. Frenklach. Kinetic modeling of soot formation with detailed chemistry and physics: Laminar premixed flames of C2 hydrocarbons. *Combustion and Flame*, 121(1–2):122–136, 2000. doi:10.1016/S0010-2180(99)00135-2.

[4] M. Balthasar. *Detailed Soot Modelling in Laminar and Turbulent Reacting Flows*. PhD thesis, Lund Institute of Technology, 2000.

[5] M. Balthasar and M. Frenklach. Detailed kinetic modeling of soot aggregate formation in laminar premixed flames. *Combustion and Flame*, 140(1–2):130–145, 2005. doi:10.1016/j.combustflame.2004.11.004.

[6] M. Balthasar and M. Kraft. A stochastic approach to calculate the particle size distribution function of soot particles in laminar premixed flames. *Combustion and Flame*, 133(3):289–298, 2003. doi:10.1016/S0010-2180(03)00003-8.

[7] M. Balthasar, F. Mauss, A. Knobel, and M. Kraft. Detailed modeling of soot formation in a partially stirred plug flow reactor. *Combustion and Flame*, 128(4):395–409, 2002. doi:10.1016/S0010-2180(01)00344-3.

[8] CD-adapco. Star-CD v4.12.003, 2009. URL `http://www.cd-adapco.com/`.

[9] M. S. Celnik, R. I. A. Patterson, M. Kraft, and W. Wagner. Coupling a stochastic soot population balance to gas-phase chemistry using operator splitting. *Combustion and Flame*, 148(3):158–176, 2007. doi:10.1016/j.combustflame.2006.10.007.

[10] M. S. Celnik, A. Raj, R. H. West, R. I. A. Patterson, and M. Kraft. Aromatic site description of soot particles. *Combustion and Flame*, 155(1–2):161–180, 2008. doi:10.1016/j.combustflame.2008.04.011.

[11] M. S. Celnik, R. I. A. Patterson, M. Kraft, and W. Wagner. A predictor-corrector algorithm for the coupling of stiff ODEs to a particle population balance. *Journal of Computational Physics*, 228(8):2758–2769, 2009. doi:10.1016/j.jcp.2008.12.030.

[12] M. S. Celnik, M. Sander, A. Raj, R. H. West, and M. Kraft. Modelling soot formation in a premixed flame using an aromatic-site soot model and an improved oxidation rate. In *Proceedings of the Combustion Institute*, volume 32, pages 639–646. The Combustion Institute, 2009. doi:10.1016/j.proci.2008.06.062.

[13] J. C. Deberry, M. Robinson, M. D. Pomponi, A. J. Beach, Y. Xiong, and K. Akhtar. Controlled vapor phase oxidation of titanium tetrachloride to manufacture titanium dioxide. U.S. Patent 6,387,347 B1, 2002. URL `http://www.google.com/patents/?id=r3gKAAAAEBAJ`.

[14] M. Denison, S. Borodai, R. Fox, and M. Bockelie. Multi-environment probability density function method for modeling turbulent combusion in industrial equipment. In *IMECE2009: Proceedings of the ASME 2009 International Mechanical Engineering Congress & Exposition*, volume 3, pages 143–149, 2010. ISBN 0-7918-4376-5. doi:10.1115/IMECE2009-12061.

[15] A. Eibeck and W. Wagner. An efficient stochastic algorithm for studying coagulation dynamics and gelation phenomena. *SIAM Journal of Scientific Computing*, 22(3): 802–821, 2000. doi:10.1137/S1064827599353488.

[16] A. Eibeck and W. Wagner. Stochastic particle approximations for Smoluchoski's coagualtion equation. *Annals of Applied Probability*, 11(4):1137–1165, 2001. doi:10.1214/aoap/1015345398.

[17] A. Eibeck and W. Wagner. Stochastic interacting particle systems and nonlinear kinetic equations. *Annals of Applied Probability*, 13(3):845–889, 2003. doi:10.1214/aoap/1060202829.

[18] R. O. Fox. *Computational Models for Turbulent Reacting Flows*. Cambridge University Press, Cambridge, 2003.

[19] M. Frenklach. Method of moments with interpolative closure. *Chemical Engineering Science*, 57(12):2229–2239, 2002. doi:10.1016/S0009-2509(02)00113-6.

[20] M. Frenklach and S. J. Harris. Aerosol dynamics modeling using the method of moments. *Journal of Colloid and Interface Science*, 118(1):252–261, 1987. doi:10.1016/0021-9797(87)90454-1.

[21] A. Garmory and E. Mastorakos. Aerosol nucleation and growth in a turbulent jet using the Stochastic Fields method. *Chemical Engineering Science*, 63(26):4078–4089, 2008. doi:10.1016/j.ces.2008.05.012.

[22] E. Gavi, D. L. Marchisio, and A. A. Baressi. CFD modelling and scale-up of confined impinging jet reactors. *Chemical Engineering Science*, 62(8):2228–2241, 2007. doi:10.1016/j.ces.2006.12.077.

[23] R. N. Ghoshtagore. Mechanism of heterogeneous deposition of thin film rutile. *Journal of the Electrochemical Society*, 117(4):529–534, 1970. doi:10.1149/1.2407561.

[24] M. Goodson and M. Kraft. An efficient stochastic algorithm for simulating nanoparticle dynamics. *Journal of Computational Physics*, 183(1):210–232, 2002. doi:10.1006/jcph.2002.7192.

[25] S. Grant, A. A. Freer, J. M. Winfield, C. Gray, T. L. Overton, and D. Lennon. An undergraduate teaching exercise that explores contemporary issues in the manufacture of titanium dioxide on the industrial scale. *Green Chemistry*, 6:25–32, 2004. doi:10.1039/b309878h.

[26] D. Grosschmidt, H. Bockhorn, M. Goodson, and M. Kraft. Two approaches to the simulation of silica particle synthesis. In *Proceedings of the Combustion Institute*, volume 29, pages 1039–1046. The Combustion Institute, 2002. doi:10.1016/S1540-7489(02)80131-6.

[27] E. Hairer and G. Wanner. *Solving Ordinary Differential Equations II. Stiff and Differential-Algebraic Problems*, volume 14 of *Springer Series in Computational Mathematics*. Springer Verlag, Berlin, 2nd revised edition, 1996.

[28] D. C. Haworth. Progress in probability density function methods for turbulent reacting flows. *Progress in Energy and Combustion Science*, 36(2):168–259, 2010. doi:10.1016/j.pecs.2009.09.003.

[29] M. C. Heine and S. E. Pratsinis. Polydispersity of primary particles in agglomerates made by coagulation and sintering. *Journal of Aerosol Science*, 38(1):17–38, 2007. doi:10.1016/j.jaerosci.2006.09.005.

[30] S. Hill. The future of titanium dioxide, market forecasts to 2016. Market report, Pira International, 2009. URL `http://www.intertechpira.com/Core/DownloadDoc.aspx?documentID=2875`.

[31] T. Johannessen, S. E. Pratsinis, and H. Livbjerg. Computational analysis of coagulation and coalescence in the flame synthesis of titania particles. *Powder Technology*, 118(3):242–250, 2001. doi:10.1016/S0032-5910(00)00401-0.

[32] J. Kee, K. Grcar, M. D. Smooke, and J. A. Miller. A Fortran program for modelling steady laminar one-dimensional premixed flames. Sandia report SAND85-8240, Sandia National Laboratories, 1985.

[33] P. Lavvas, M. Sander, M. Kraft, and H. Imanaka. Surface chemistry and particle shape. Processes for the evolution of aerosols in Titan's atmosphere. *The Astrophysical Journal*, 728(2):80, 2011. doi:10.1088/0004-637X/728/2/80.

[34] P. A. Libby and F. A. Williams. *Turbulent Reacting Flows*. Springer-Verlag, Berlin, 1980. ISBN 3-540-10192-6.

[35] D. L. Marchisio and R. O. Fox. Solution of population balance equations using the direct quadrature method of moments. *Journal of Aerosol Science*, 36(1):43–73, 2005. doi:10.1016/j.jaerosci.2004.07.009.

[36] R. McGraw. Description of aerosol dynamics by the quadrature method of moments. *Aerosol Science and Technology*, 27(2):255–349, 1997. doi:10.1080/02786829708965471.

[37] M. Mehta, Y. Sung, V. Raman, and R. O. Fox. Multiscale modeling of TiO_2 nanoparticle production in flame reactors: Effect of chemical mechanism. *Industrial & Engineering Chemistry Research*, 49(21):10663–10673, 2010. doi:10.1021/ie100560h.

[38] N. Morgan, C. Wells, M. Kraft, and W. Wagner. Modelling nanoparticle dynamics: coagulation, sintering, particle inception and surface growth. *Combustion Theory and Modelling*, 9(3):449–461, 2005. doi:10.1080/13647830500277183.

[39] N. Morgan, C. G. Wells, M. J. Goodson, M. Kraft, and W. Wagner. A new numerical approach for the simulation of the growth of inorganic nanoparticles. *Journal of Computational Physics*, 211(23):638–658, 2006. doi:10.1016/j.jcp.2005.04.027.

[40] N. Morgan, M. Kraft, M. Balthasar, D. Wong, M. Frenklach, and P. Mitchell. Numerical simulations of soot aggregation in premixed laminar flames. In *Proceedings of the Combustion Institute*, volume 31, pages 693–700. The Combustion Institute, 2007. doi:10.1016/j.proci.2006.08.021.

[41] A. J. Morris and M. D. Coe. System for increasing the capacity of a titanium dioxide producing process. U.S. Patent 4,803,056, 1989. URL `http://www.google.com/patents/?id=R805AAAAEBAJ`.

[42] M. E. Mueller, G. Blanquart, and H. Pitsch. A joint volume-surface model of soot aggregation with the method of moments. In *Proceedings of the Combustion Institute*, volume 32, pages 785–792. The Combustion Institute, 2009. doi:10.1016/j.proci.2008.06.207.

[43] R. I. A. Patterson, J. Singh, M. Balthasar, M. Kraft, and J. Norris. The linear process deferment algorithm: A new technique for solving population balance equations. *SIAM Journal on Scientific Computing*, 28(1):303–320, 2006. doi:10.1137/040618953.

[44] R. I. A. Patterson, J. Singh, M. Balthasar, M. Kraft, and W. Wagner. Extending stochastic soot simulation to higher pressures. *Combustion and Flame*, 145(3):638–642, 2006. doi:10.1016/j.combustflame.2006.02.005.

[45] N. Peters. *Turbulent Combustion*. Cambridge University Press, Cambridge, 2000.

[46] S. B. Pope. PDF methods for turbulent reacting flows. *Progress in Energy and Combustion Science*, 11(2):119–192, 1985. doi:10.1016/0360-1285(85)90002-4.

[47] S. E. Pratsinis. Simultaneous nucleation, condensation, and coagulation in aerosol reactors. *Journal of Colloid and Interface Science*, 124(2):416–427, 1988. doi:10.1016/0021-9797(88)90180-4.

[48] S. E. Pratsinis. Flame aerosol synthesis of ceramic powders. *Progress in Energy and Combustion Science*, 24(3):197–219, 1998. doi:10.1016/S0360-1285(97)00028-2.

[49] S. E. Pratsinis and P. T. Spicer. Competition between gas phase and surface oxidation of $TiCl_4$ during synthesis of TiO_2 particles. *Chemical Engineering Science*, 53(10): 1861–1868, 1998. doi:10.1016/S0009-2509(98)00026-8.

[50] S. E. Pratsinis, H. Bai, P. Biswas, M. Frenklach, and S. V. R. Mastrangelo. Kinetics of titanium (IV) chloride oxidation. *Journal of the Americam Ceramic Society*, 73 (7):2158–2162, 1990. doi:10.1111/j.1151-2916.1990.tb05295.x.

[51] S. E. Pratsinis, S. Vemury, G. P. Fotou, and A. Gutsch. Process for producing ceramic powders, especially titanium dioxide useful as a photocatalyst. U.S. Patent 5,698,177, 1997. URL `http://www.google.com/patents/?id=OgwfAAAAEBAJ`.

[52] D. Ramkrishna. *Population Balances — Theory and Applications to Particulate Systems in Engineering*. Academic Press, San Diego, 2000.

[53] K. L. Revzan, N. J. Brown, and M. Frenklach. Soot formation codes, 1999. URL `http://www.me.berkeley.edu/soot`.

[54] S. Rigopoulos. PDF method for population balance in turbulent reactive flow. *Chemical Engineering Science*, 62(23):6865–6878, 2007. doi:10.1016/j.ces.2007.05.039.

[55] S. Rigopoulos. Population balance modelling of polydispersed particles in reactive flows. *Progress in Energy and Combustion Science*, 36(4):412–443, 2010. doi:10.1016/j.pecs.2009.12.001.

[56] D. E. Rosner. Flame synthesis of valuable nanoparticles: Recent progress/current needs in areas of rate laws, population dynamics, and characterization. *Industrial & Engineering Chemistry Research*, 44(16):6045–6055, 2005. doi:10.1021/ie0492092.

[57] P. Roth. Particle synthesis in flames. In *Proceedings of the Combustion Institute*, volume 31, pages 1773–1788. The Combustion Institute, 2007. doi:10.1016/j.proci.2006.08.118.

[58] P. G. Saffman and J. S. Turner. On the collision of drops in turbulent clouds. *Journal of Fluid Mechanics*, 1(1):16–30, 1956. doi:10.1017/S0022112056000020.

[59] M. Sander, R. H. West, M. S. Celnik, and M. Kraft. A detailed model for the sintering of polydispersed nanoparticle agglomerates. *Aerosol Science and Technology*, 43 (10):978–989, 2009. doi:10.1080/02786820903092416.

[60] M. Sander, R. I. A. Patterson, A. Braumann, A. Raj, and M. Kraft. Developing the PAH-PP soot particle model using process informatics and uncertainty propagation. In *Proceedings of the Combustion Institute*, volume 33, pages 675–683. The Combustion Institute, 2011. doi:10.1016/j.proci.2010.06.156.

[61] T. Seto, A. Hirota, T. Fujimoto, M. Shimada, and K. Okuyama. Sintering of polydisperse nanometer-sized agglomerates. *Aerosol Science and Technology*, 27(3): 422–438, 1997. doi:10.1080/02786829708965482.

[62] R. Shirley, Y. Liu, T. S. Totton, R. H. West, and M. Kraft. First-principles thermochemistry for the combustion of a $TiCl_4$ and $AlCl_3$ mixture. *Journal of Physical Chemistry A*, 113(49):13790–13796, 2009. doi:10.1021/jp905244w.

[63] R. Shirley, J. Akroyd, L. A. Miller, O. Inderwildi, U. Riedel, and M. Kraft. Theoretical insights into the surface growth of rutile TiO_2. Technical Report 100, c4e-Preprint Series, Cambridge, 2011. URL `http://como.cheng.cam.ac.uk/index.php?Page=Preprints`. Submitted to *Combustion and Flame*.

[64] J. Singh, M. Balthasar, M. Kraft, and W. Wagner. Stochastic modeling of soot particle size and age distributions in laminar premixed flames. In *Proceedings of the Combustion Institute*, volume 30, pages 1457–1465. The Combustion Institute, 2005. doi:10.1016/j.proci.2004.08.120.

[65] P. T. Spicer, O. Chaoul, S. Tsantilis, and S. E. Pratsinis. Titania formation by $TiCl_4$ gas phase oxidation, surface growth and coagulation. *Journal of Aerosol Science*, 33 (1):17–34, 2002. doi:10.1016/S0021-8502(01)00069-6.

[66] G. Strang. On the construction and comparison of difference schemes. *SIAM Journal on Numerical Analysis*, 5(3):506–517, 1968. doi:10.1137/0705041.

[67] Q. Tang, W. Zhao, M. Bockelie, and R. O. Fox. Multi-environment probability density function method for modelling turbulent combustion using realistic chemical kinetics. *Combustion Theory and Modelling*, 11(6):889–907, 2007. doi:10.1080/13647830701268890.

[68] S. Tsantilis and S. E. Pratsinis. Narrowing the size distribution of aerosol-made titania by surface growth and coagulation. *Journal of Aerosol Science*, 35(3):405–420, 2004. doi:10.1016/j.jaerosci.2003.09.006.

[69] G. d. Veroli and S. Rigopoulos. Modeling of turbulent precipitation: A transported population balance-PDF method. *AIChE Journal*, 56(4):878–892, 2010. doi:10.1002/aic.12064.

[70] J. Villermaux and J. C. Devillon. Représentation de la coalescence et de la redispersion des domaines de ségrégation dans un fluide par un modèle d'interaction

phénoménologique. In *Proceedings of the 2nd International Symposium on Chemical Reaction Engineering*, pages 1–13. International Symposium on Chemical Reaction Engineering, Elsevier, New York, 1972.

[71] L. Wang and R. O. Fox. Comparison of micromixing models for CFD simulation of nanoparticle formation. *AIChE Journal*, 50(9):2217–2232, 2004. doi:10.1002/aic.10173.

[72] C. G. Wells. A stochastic approximation scheme and convergence theorem for particle interactions with perfectly reflecting boundary conditions. *Monte Carlo Methods and Applications*, 12(3):291–342, 2006. doi:10.1163/156939606778705182.

[73] C. G. Wells and M. Kraft. Direct simulation and mass flow stochastic algorithms to solve a sintering-coagulation equation. *Monte Carlo Methods and Applications*, 11 (2):175–197, 2005. doi:10.1515/156939605777585980.

[74] C. G. Wells, N. Morgan, M. Kraft, and W. Wagner. A new method for calculating the diameters of partially-sintered nanoparticles and its effect on simulated particle properties. *Chemical Engineering Science*, 61(1):158–166, 2006. doi:10.1016/j.ces.2005.01.048.

[75] R. H. West, G. J. O. Beran, W. H. Green, and M. Kraft. First-principles thermochemistry for the production of TiO_2 from $TiCl_4$. *Journal of Physical Chemistry A*, 111(18):3560–3565, 2007. doi:10.1021/jp0661950.

[76] R. H. West, M. S. Celnik, O. R. Inderwildi, M. Kraft, G. J. O. Beran, and W. H. Green. Toward a comprehensive model of the synthesis of TiO_2 particles from $TiCl_4$. *Industrial & Engineering Chemistry Research*, 46(19):6147–6156, 2007. doi:10.1021/ie0706414.

[77] R. H. West, R. Shirley, M. Kraft, C. F. Goldsmith, and W. H. Green. A detailed kinetic model for combustion synthesis of titania from $TiCl_4$. *Combustion and Flame*, 156(9):1764–1770, 2009. doi:10.1016/j.combustflame.2009.04.011.

[78] D. L. Wright Jr, R. McGraw, and D. E. Rosner. Bivariate extension of the quadrature method of moments for modeling simultaneous coagulation and sintering of particle populations. *Journal of Colloid and Interface Science*, 236(2):242–251, 2001. doi:10.1006/jcis.2000.7409.

[79] B. Zhao, Z. Yang, M. V. Johnston, H. Wang, A. S. Wexler, M. Balthasar, and M. Kraft. Measurement and numerical simulation of soot particle size distribution functions in a laminar premixed ethylene-oxygen-argon flame. *Combustion and Flame*, 133(1–2):173–188, 2003. doi:10.1016/S0010-2180(02)00574-6.

[80] A. Zucca, D. L. Marchisio, M. Vanni, and A. A. Barresi. Validation of bivariate DQMoM for nanoparticle simulation. *AIChE Journal*, 53(4):918–931, 2007. doi:10.1002/aic.11125.

Citation index